PHYSICAL REVIEW A VOLUME 19, NUMBER 2 FEBRUARY 1979

Projectile Auger spectra of gas- and foil-excited oxygen ions at MeV energies

R. Bruch
Fakultät für Physik, Universität Freiburg, D-7800 Freiburg, West Germany

D. Schneider
Hahn-Meitner-Institut für Kernforschung Berlin, 1000 Berlin 39, West Germany

W. H. E. Schwarz* and M. Meinhart
Lehrstuhl für Theoretische Chemie, Universität Bonn, D-5300 Bonn, West Germany

B. M. Johnson
Brookhaven National Laboratory, Upton, New York 11973

K. Taulbjerg
Institute of Physics, University of Aarhus, DK-8000 Aarhus C, Denmark
(Received 24 April 1978)

High-resolution projectile Auger spectra of singly and doubly core-excited oxygen ions are studied as a function of incident beam energy (2–18 MeV), exciter gas (helium, neon, argon, and krypton) or foil (carbon), incident charge state (1+ to 4+), and delay time. Auger-electron production from excited oxygen states varies considerably for collisions with different beam energies and exciter gases. A striking similarity in both the linewidths and relative Auger line intensities is observed for single-collision gas and multiple-collision foil excitation. The incident ion charge state does not appreciably affect the excitation cross sections and the charge state of the outgoing projectile. In order to assign the measured Auger peaks numerous excitation and Auger transition energies for singly and doubly core-excited states are calculated using semiempirical and *ab initio* methods. Calculated transition energies are compared with experimental line structures. Possible excitation and deexcitation mechanisms are suggested and discussed within a quasimolecular single-particle model.

I. INTRODUCTION

Detailed information concerning the atomic structure of highly excited and ionized atoms is obtained from high-resolution measurements of Auger electrons produced by heavy ion bombardment.[1-10] In particular, measurements of the relative Auger yield of specific core-excited states as a function of beam energy, exciter target (i.e., gas or foil), initial charge state, and observation angle can give additional information with respect to the ion-atom excitation mechanism.[2,11]

Until recently, high-resolution measurements of Auger electron production in ion-atom collisions were mainly restricted to light ion bombardment.[12-14] In Auger electron spectra for 30-MeV $O^{n+}-O_2$ collisions reported by Stolterfoht *et al.*,[15] the energy resolution was not sufficient to resolve individual projectile Auger lines. Although individual lines attributed to the decay of metastable oxygen and fluorine states were resolved in delayed emission beam-foil measurements (summarized in articles by Pegg *et al.*[16] and Sellin *et al.*[17]), attempts to measure prompt beam Auger electrons by directly viewing the back of a foil were hampered by enhanced line broadening and many overlapping Auger features.

Schneider *et al.*[18] measured high-resolution spectra from 2-MeV C^+ ions excited by collisions with thin carbon foils or Ne target gas. A comparison of the prompt C projectile electron spectra indicated a striking similarity of excitation and ionization processes for multiple-collision beam-foil and single-collision beam-gas excitation.

Quite recently charge distributions of oxygen ions after small-impact-parameter collisions between O^{n+} and rare gases were studied by Rosner *et al.*[19,20] These measurements indicated that for the heavier gases equilibrium charge distribution may be attained under single collision conditions. Thus Rosner *et al.* observed average outgoing charges after a single collision as high as those measured after the passage through foils. Another surprising result of this study was the insensitivity of the outgoing charge-state distribution on the initial projectile charge state, especially for the heavier target gases.

High-resolution measurements of the Auger decay of energetic oxygen ions excited by collisions with noble gases and foils are the subject of this work. In the present study, kinematic scattering is reduced and energy straggling of the ion beam in the foil is avoided using a thin gas target so that projectile electron emission is measured under

single collision conditions. By selecting small observation angles with respect to the incident ion beam, we further reduced the observed line widths.[7,21-23]

In addition to the work of Schneider *et al.*[6,10,18] we present here oxygen projectile Auger spectra as a function of incident beam energy, exciter gas or foil, incident charge state and delay time. Individual prompt Auger transitions from fast moving oxygen beams are partially resolved and compared with theoretical calculations. Our measurements show that the Auger structures are rather insensitive with respect to the initial charge state, and that the foil-excited Auger spectra are very similar to gas-excited spectra, in particular for target gases with higher Z.[23]

The experimental setup is described in Sec. II and the experimental results are presented in Sec. III. In order to assign the most prominent Auger features we performed theoretical estimates and *ab initio* calculations which are discussed in Sec. IV. A comparison of the experimental data with theoretical results is given in Sec. V. Finally, Sec. VI is devoted to specific excitation and deexcitation processes.

II. EXPERIMENTAL PROCEDURE

Figure 1 shows the experimental setup for high-resolution projectile Auger-electron detection.[23] Oxygen ion beams were produced by the University of Texas at Austin model EN Van de Graaff accelerator. The energy and charge state of the beam were determined by a calibrated analyzing magnet. Since the laboratory energies of beam Auger electrons depend sensitively on the projectile velocity, the analyzing magnet was carefully calibrated to ensure accurate determination of beam energies to within 0.3%. Beam dispersion (angular spread of the beam) in the collision region was less than 0.2%.

For the beam-gas measurements, a grounded tantalum aperture (1 mm in diameter), placed in front of the gas-jet holder, excluded stray particles from entering the collision region; then two biased tantalum apertures (of increasingly larger diameters) removed any stray electrons that may have been traveling with the beam or produced at the ground aperture. The oxygen ions then crossed diffuse target gas beams of He, Ne, Ar, or Kr at a distance of 3 mm from a 0.3-mm gas nozzle.

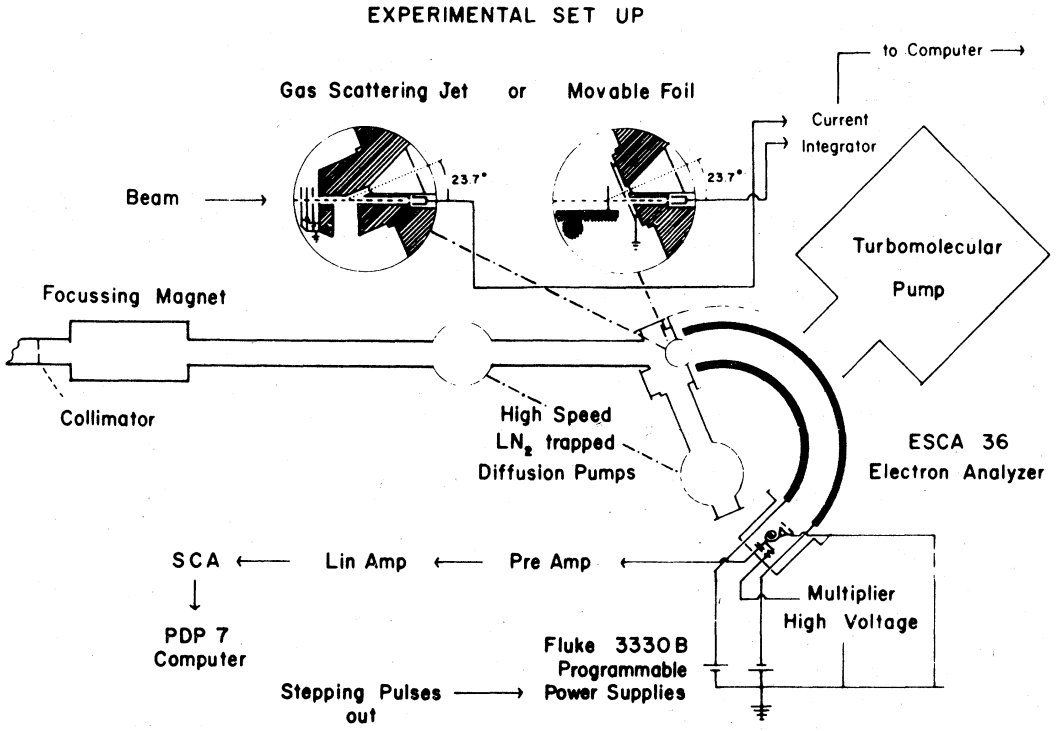

FIG. 1. Diagram of the experimental arrangement used for detecting beam Auger electrons at a laboratory emission angle of 23.7°. For beam-gas and beam-foil measurements the interchangeable "Gas Scattering Jet" and "Movable Foil" apparatus (shown in the inset circles) were attached at the entrance to the spectrometer.

After leaving the collision region, the beam finally passed through a 2-mm grounded aperture and was collected in a small Faraday cup electrically floating at 80 V (see "Gas Scattering Jet" inset in Fig. 1).

The pressure during each run was maintained at about a few 10^{-3} Torr in the collision region, at about 1×10^{-4} Torr a few cm from the gas jet, and at less than 5×10^{-6} Torr inside the spectrometer. Relative intensities of spectral features were measured as a function of gas pressure to ensure single collision conditions.

For the beam-foil measurements, the oxygen ions passed through thin carbon foils of nominal thickness 5 $\mu g/cm^2$. The foil could be moved from zero distance (i.e., within the analyzer viewing region) to about 5 cm upstream. This allowed the study of delayed electron emission as a function of distance downstream from the exciter foil. A grounded preentrance slit 10.2×1.0 mm was placed in front of the primary entrance slit to the spectrometer to reduce the number of scattered electrons at the analyzer entrance (see "Movable Foil" inset in Fig. 1).

The analyzer and collision regions were shielded against stray magnetic fields with double layers of Permalloy. Residual magnetic field strengths were determined to be less than 1 mG within the analyzer and less than 10 mG in the collision region.

Electrons ejected from the beam-gas collision at a lab emission angle (θ_L) of 23.7° were energy analyzed with a double focussing electrostatic analyzer (McPherson ESCA-36). The intrinsic resolution of the spectrometer was 0.02% full width at half maximum (FWHM). Energy and efficiency calibrations of the spectrometer had been accomplished[24] by substituting an electron gun for the Van de Graaff accelerator and performing elastic scattering measurements as well as comparing Ne-KLL Auger line energies and intensities (for $\theta_L = 90°$) with the e^- +Ne data of Krause *et al.*[25] Due to kinematic line broadening effects, the obtained energy resolution in this experiment was degraded to about 0.6% FWHM (see Table I).

The data-acquisition system, controlled by a PDP 7 computer, has been described in detail elsewhere.[23,24] Data were accumulated in a single channel of computer memory until a fixed number of μC had been collected in the Faraday cup. The typical accumulation time per channel was about 1 sec. Several runs were taken for each beam energy, incident ion charge state, and exciter gas or foil. After assuring that no energy shifts or changes in relative line intensities had occurred, corresponding runs were added to improve statistics.

III. EXPERIMENTAL RESULTS

A. Energy, exciter gas and charge-state dependence

The Auger decay of the oxygen ions was studied as a function of exciter gas (helium, neon, argon, or krypton), incident beam energy (2–18 MeV), and incident ion charge state (1+ to 4+).

1. Energy dependence

Figure 2 shows the energy dependence of oxygen Auger electron emission for O^{n+}–Ne bombardment. As can be seen the strength of spectral features shifts to lower energies for higher beam energies and higher initial charge states. Higher beam energies, in general, produce higher degrees of multiple ionization. We further note that the observed linewidths increase considerably with beam energy.

TABLE I. Comparison of estimated kinematic broadening to measured peak widths.

Dependence	Ion	Energy (MeV)	Exciter	Kinematic line broadening $\Delta E/E$ (%) $\Delta E_{\theta_L}/E$[a]	$\Delta E_K/E$[b]	comb[c]	Measured peak width
	0^+	2	He	0.52	0.07	0.52	0.5
Exciter	0^+	2	Ne	0.52	0.35	0.62	0.6
gas	0^+	2	Ar	0.52	0.63	0.81	0.9
	0^+	2	Kr	0.52	1.27	1.37	1.5
	0^+	2	Ne	0.52	0.35	0.62	0.6
Beam	0^{2+}	5	Ne	0.71	0.13	0.73	0.8
energy	0^{2+}	8	Ne	0.83	0.08	0.84	1.0
	0^{3+}	18	Ne	1.1	0.03	1.1	1.3
Charge state	1,2,3,4+	5	Ne	0.71	0.13	0.73	0.9

[a] Estimated broadening $\Delta E_{\theta_L}/E$ due to the finite spectrometer acceptance angles (Ref. 21).
[b] Estimated kinematic (Doppler) broadening $\Delta E_K/E$ (Ref. 21).
[c] Combined effects of $\Delta E_{\theta_L}/E$ and $\Delta E_K/E$ computed as $[(\Delta E_{\theta_L})^2 + (\Delta E_K)^2]^{1/2}/E$.

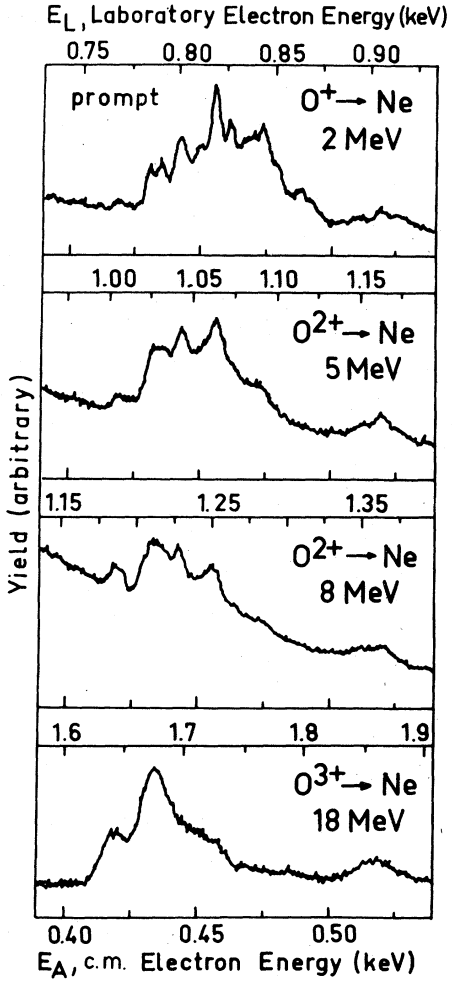

FIG. 2. Beam-gas Auger electron emission spectra for 2-MeV O^+, 5-MeV O^{2+}, 8-MeV O^{2+}, and 18-MeV O^{3+} ions excited by collisions with Ne (recorded at $\theta_L = 23.7°$). Energy scales are normalized to the ionic rest frame electron energies (E_A). Measured laboratory electron energies (E_L) are also given to demonstrate the transformation to higher laboratory energies as the incident energy is increased.

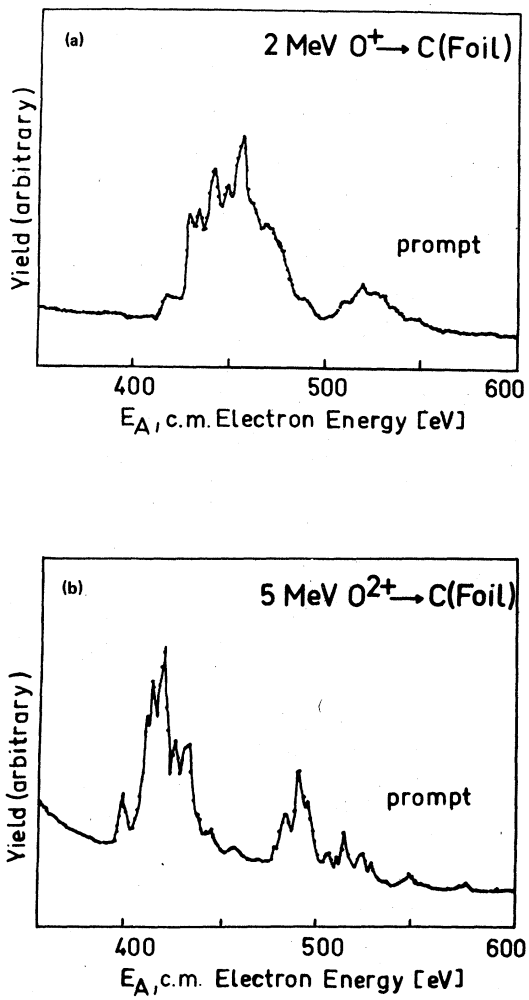

FIG. 3. Comparison of Auger electron emission spectra for (a) 2-MeV O^+ and (b) 5-MeV O^{2+} ions excited by collisions with carbon foils.

In Fig. 3(a) and 3(b), representative 2-MeV O^+ on C-foil and a 5-MeV O^{2+} on C-foil spectra are displayed. Since the foil region is viewed directly by the analyzer, prompt transitions are measured. However, due to the finite acceptance length of the spectrometer, a small percentage of the decay of metastable states is also observed. The spectral features in Figs. 3(a) and 3(b) originate mainly from the decay of three-to-six electron oxygen ions (see Sec. V).

2. *Exciter gas dependence*

In Fig. 4, 2-MeV O^+ on He, Ne, Ar, and Kr spectra are shown. Some qualitative features are noted. First, the overall structure in the spectra is shifted to lower energies for collisions with heavier target atoms, i.e., heavier exciter gases generally produce higher degrees of multiple ionization. Second, increased line broadening is observed for heavier target gases.

3. *Charge-state dependence*

Figure 5 shows the charge-state dependence for beam-gas Auger electron emission in 5-MeV O^{n+} $\rightarrow$Ne collisions for $n = 1$–4. The spectra exhibit little change in strength or broadening of spectral features. The lack of a pronounced charge-state dependence indicates that the degree of ionization produced in these collisions is nearly the same. Thus, it appears that for the 2-MeV collisions investigated, the incident-ion charge-state does not appreciably affect the charge-state distributions

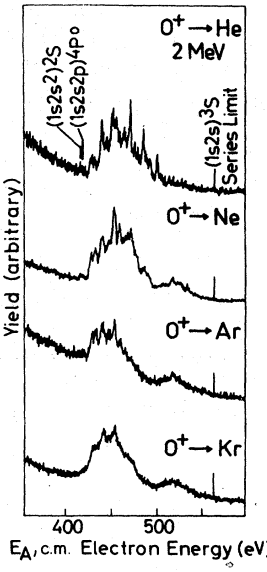

FIG. 4. Beam-gas Auger electron emission spectra for 2-MeV O^+ ions excited by collisions with He, Ne, Ar, and Kr (recorded at $\theta_L = 23.7°$).

after the collision. Assuming that ionization processes are more probable than electron capture to lower charge states, this implies that most of the observed lines correspond to transitions from highly ionized initial states. Comparison of measured line energies with calculated transition energies (see Secs. IV and V) is consistent with this assumption.

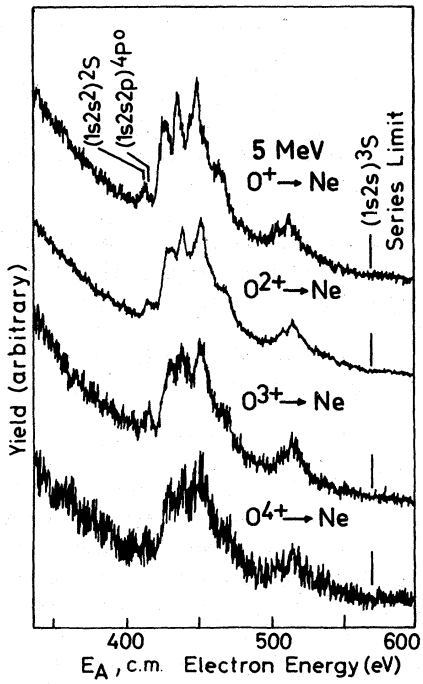

FIG. 5. Beam-gas Auger electron emission spectra for 5-MeV O^+, O^{2+}, O^{3+}, and O^{4+} ions excited by collisions with Ne (recorded at $\theta_L = 23.7°$).

B. Comparison of gas- and foil-excited spectra

Figure 6 shows spectra for 2-MeV O^+ ions excited by collisions with (i) Ne gas and (ii) carbon foil (5 $\mu g/cm^2$). Both spectra were recorded with the analyzer directly viewing the collision region. For the beam-foil spectrum this was accomplished by adjusting the foil position until a maximum yield was detected.

The similarity in the spectra of Fig. 6 is a striking result. We note that the measured line widths are nearly identical for single collision $O^+ \rightarrow$ Ne as opposed to multiple $O^+ \rightarrow$ C-foil collisions for 2$\frac{1}{2}$ MeV beam energy. This is surprising because multiple scattering and energy straggling in the foil should increase line broadening. It is concluded, therefore, that broadening effects not associated with beam scattering are dominant for 2-MeV $O^+ \rightarrow$ Ne and $O^+ \rightarrow$ C-foil collisions. Furthermore Fig. 6 seems to indicate that ions which emerge from the foil with a K-shell vacancy have nearly the same degree of L-shell vacancies as ions which have undergone a single ion-atom collision. This observation is consistent with the Auger data of Schneider *et al.*[18]

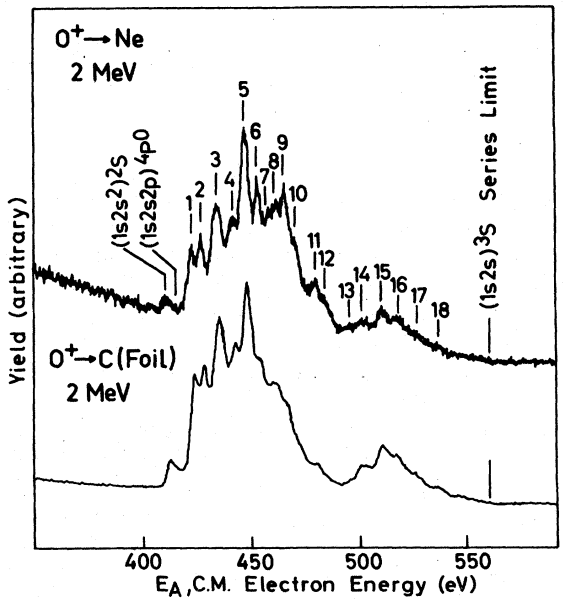

FIG. 6. Comparison of beam Auger electron emission (recorded at $\theta_L = 23.7°$) for 2-MeV O^+ ions excited by collisions with (a) Ne and (b) a thin carbon foil. The similarity of qualitative features for the $O^+ \rightarrow$ C-foil and $O^+ \rightarrow$ Ne spectra indicates the similarity of ionization mechanisms for beam foil and beam gas excitation. The $O^+ \rightarrow$ C-foil spectrum has been shifted to slightly higher energies to compensate for beam energy loss in the foil.

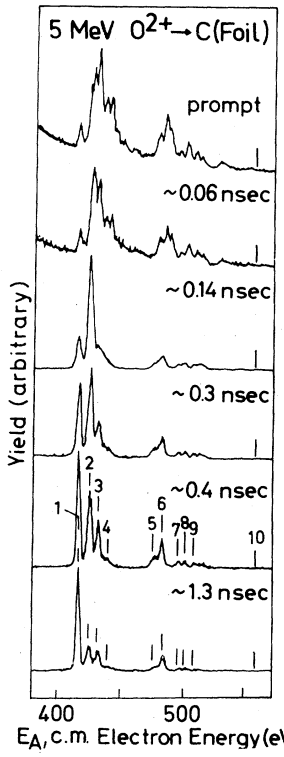

FIG. 7. Prompt and delayed emission beam Auger electron spectra (recorded at $\theta_L = 23.7°$) for 5-MeV O^{2+} ions excited by passing through a thin carbon foil (see Table VI.

C. Time-delayed spectra

In heavy ion-atom collisions high states of multiple ionization and excitation are produced. Many excited states of multiply ionized atoms can decay promptly by either x-ray or Auger-electron emission, but a surprisingly large number of highly excited states are metastable to either or both of these decay processes. Figure 7 shows prompt and delayed electron spectra for 5-MeV O^{2+} ions excited by collisions with carbon foils. Peaks strongly observed in the delayed emission spectra (labeled 1 through 10 in the figure) are attributed to transitions from metastable states. Prompt transitions (not numbered) in the zero delay spectrum are diminished as the foil is moved upstream. The line identification of the delayed spectra is discussed in Sec. V.

D. Peak widths

In Table I estimated peak widths for all of the spectra displayed in Figs. 2–7 are given. The observed widths are compared to line-broadening effects due to finite acceptance angle of the spectrometer $\Delta E_{\theta_L}/E$ and Doppler line broadening $\Delta E_K/E$. We also estimated the combined effect (added in quadrature) of these two contributions.[21,22] Table I shows that the changes in spectral resolution are in good agreement with the assumption that ΔE_{θ_L} and ΔE_K are the dominant contributions to line broadening.

IV. THEORETICAL ENERGY LEVELS

A. Hartree-Fock calculations

In order to establish the energy-level schemes, which are relevant to the experimental spectra, we have calculated highly excited autoionizing states in oxygen using semiempirical and *ab initio* methods. Thus, nearly all singly and doubly core-excited $K^m L^n$ terms of oxygen ions with charges 1–6 were estimated. First we have determined nonrelativistic restricted *Hartree-Fock* (NRHF) energies with the Froese-Fischer code.[26] For details see Ref. 27. The accuracy of these energy values is in the eV range. Second, the energies of single and double K-shell hole states have been computed semiempirically with the *equivalent core model*[28,29] using the relations

$$E(O^{1s^1}[2s^i 2p^{jM}L]^{M+1}L) = E(F^{1s^2}[2s^i 2p^{jM}L]^M L) - E(F^{7+}1s^2) + E(O^{7+}1s) + \Delta^{\pm}_{SCF}, \quad (1)$$

$$E(OL^{nM}L) = E(Ne^{1s^2}2s^i 2p^{jM}L) - E(Ne^{8+}1s^2) + \Delta_{SCF},$$

where the energies E on the right-hand side of Eqs. (1) are known experimentally.[30,31] Δ_{SCF} is the difference of the NRHF interaction energies between the L-shell and the different cores $F^{7+}1s^2$, $O^{7+}1s$ and $Ne^{8+}1s^2$, O^{8+}, respectively. Δ_{SCF} contains the nuclear attraction integral $\langle L|1/r|L\rangle$ and the Coulomb and exchange integrals J_{KL} and K_{KL}; e.g., for $O1s(2s2p\,^3P^0)^2P^0$

$$\Delta_{SCF} = (\langle 2s|1/r - J_{1s}|2s\rangle + \langle 2p|1/r - J_{1s}|2p\rangle) + \tfrac{3}{2}(K_{1s2s} + K_{1s2p}) \quad (2a)$$

and for $O(2s^2)^1S$

$$\Delta_{SCF} = 4\langle 2s|1/r - J_{1s}|2s\rangle + 2K_{1s2s}. \quad (2b)$$

Since the predicted energies are based on experimental data, relativistic and correlation effects are empirically accounted for. The excitation energies determined in this manner are expected to be accurate within an eV.

In Table II we have collected the lowest possible Auger transition energies associated with the $K^1L^n \to K^2L^{n-2} + e$ and the $K^0L^n \to K^1L^{n-2} + e$ decay processes. As can be seen, transition energies

TABLE II. Lowest possible K Auger transition energies originating from singly and doubly core-excited oxygen ions. Energies are given in eV.

Ion		Type of autoionization processes[a] $K^1L^n \rightarrow K^2L^{n-2}$ ECM	NRHF	$K^0L^n \rightarrow K^1L^{n-2}$ ECM	NRHF
O^{6+}	(He-like)			463	464
O^{5+}	(Li-like)	413	415	472	476
O^{4+}	(Be-like)	425	426	482	487
O^{3+}	(B-like)	436	435	498	497
O^{2+}	(C-like)		448	510	511
O^{+}	(N-like)		459		

[a] ECM: equivalent core model; NRHF: nonrelativistic restricted Hartree-Fock calculations.

calculated with the equivalent core model are in general lower than the corresponding NRHF energy values, due to the missing relativistic and correlation energies in the latter case. Since the nuclear charge is less shielded in K^0L^n than in K^1L^n states (by nearly one unit), more energy (about 50 eV) is released in $K^0L^n \rightarrow K^1L^{n-2} + e$ than in $K^1L^n \rightarrow K^2L^{n-2} + e$ Auger decays. We further note that the interelectronic repulsion increases with the number n of L-electrons; therefore Auger transition energies increase (by roughly 10–15 eV) if n is increased by one. We also mention that the energy range of possible KLL Auger transition energies associated with a specific initial K^mL^n configuration ($m=0$ or $m=1$) increases from about 1 a.u. for $n=2$ to about 3 a.u. for $n=6$. Consequently the Auger features arising from different initial configurations are overlapping significantly.

B. Multiconfiguration calculations

We also performed *ab initio* calculations on singly and doubly core-excited states using the generalized Brillouin theorem (GBT) *multiconfiguration method* (MC) of Chang and Schwarz.[6,32,33] In brief, the wave function is approximated by

$$\psi = \sum_{n=1}^{N} C_n \psi_n(\varphi_i) . \tag{3}$$

(φ_i) is a set of atomic orbitals (AO's), ψ_n is an LS configuration formed from these orbitals, and C_n is a linear variational coefficient. The AO's were expanded in a slightly contracted $12s/7p$ Gaussian orbital basis of Duijneveldt[34] augmented by two sets of d functions with exponents 2.5 and 0.8. The AO's φ_i and the configuration mixing coefficients C_n are simultaneously optimized in a variational calculation. This is achieved by diagonalizing the so-called super-CI matrix.[32,33] Since this procedure guarantees orthogonality of the orbitals and wave functions only to first order, it is necessary after each super-CI step to Schmidt-orthogonalize the orbitals φ_i and to correct the C_n by a small $N \times N$ CI calculation.

Besides the leading configuration the following ones are included in expansion (3) (see Table III):

(i) internal correlation configurations (terms belonging to the same complex);

(ii) the most important semi-internal configurations, i.e., those ones which differ in spin or orbital momentum coupling from the leading configuration;

(iii) configurations important for variational stability of highly excited states but not already intrinsically accounted for by the GBT-MC technique.[32,33] We found that K^2L^{n-2} configurations have a negligible effect on K^0L^n states. Also the much lower-lying $K^{m+1}L^{n-2}$ M-Rydberg configurations can be neglected for the determination of K^mL^n states.

The calculated energies are semiempirically corrected for external correlation using the pair energy increments of Öksüz and Sinanoğlu.[35] Finally it is necessary to account for the relativistic energy contribution, which is of the order of an eV. This was achieved on the basis of data given in the literature.[36-38] The results are presented in Table III along with previous calculations.[39-41] We expect our K^0L^n and K^1L^n energies to be accurate within a few tenths of an eV.

C. Rydberg states

Finally, to obtain estimates of core-excited Rydberg states we again applied the *equivalent core model*. For example,

$$E(OK^0L^m nl) = E(NeK^2L^m nl) - E(NeK^2L^m) + E(OK^0L^m) + \Delta_{SCF} . \tag{4a}$$

In the case of OK^1 versus FK^2 states one has to take account of the correct parentages, e.g.,

TABLE III. MC calculations of several normal and singly and doubly core-excited states of O^{n+}.

No. of electrons	Term	Leading configuration[a]	Additional configurations[a]	Total No. of configs.	Calc. energy in a.u.	Corrected for ext. correlation and relativity	Deviation in eV from experiment[b]	Deviation in eV from $1/Z$ expansion[c]
2	^1S	$1s^2$		1	−59.111	−59.199	−0.1	−0.1
3	^2S	$1s^2 2s$		1	−64.178	−64.271	0.0	−0.1
4	^1S	$1s^2 2s^2$	$1s^2 2p^2$	2	−68.355	−68.460	−0.1	
5	$^2P^o$	$1s^2 2s^2 2p$	$1s^2 2p^3, 1s^2 2s 2p 3d(2)$	4	−71.178	−71.303	−0.1	
3	^2S	$1s 2s^2$	$1s^2 2s, 1s 2p^2$	3	−43.978	−44.025		0.1
3	^4S	$1s 2s 3s$	$1s 2p 3p$	2	−40.861	−40.893		0.0[d]
3	^2S	$1s 2s 3s(2)$	$1s^2 2s, 1s^2 3s, 1s 2s^2, 1s 2p^2, 1s 2p 3p(2)$	8	−40.754	−40.786		
3	^2S	$1s 2s 3s(2)$	$1s^2 2s, 1s^2 3s, 1s 2s^2, 1s 2p^2, 1s 2p 3p(2)$	8	−40.541	−40.576		
4	$^3P^o$	$1s 2s^2 2p$	$1s^2 2s 2p, 1s 2p^3, 1s 2s 2p 3d(3)$	6	−48.173	−48.238		0.4
4	$^1P^o$	$1s 2s^2 2p$	$1s^2 2s 2p, 1s 2p^3, 1s 2s 2p 3d(2)$	5	−48.009	−48.078		0.2
4	^5P	$1s 2s 2p^2$		1	−48.096	−48.146		0.0
4	^3S	$1s 2s 2p^2$	$1s^2 2s 3s, 1s 2s^2 3s$	3	−47.475	−47.569		0.0
4	^1S	$1s 2s 2p^2$	$1s^2 2s^2, 1s^2 2p^2, 1s 2s^2 3s$	4	−47.224	−47.322		0.3
2	^1S	$2s^2$	$1s 2s, 2p^2$	3	−15.039	−15.063		−0.3[e]
4	^3P	$2s^2 2p^2$	$1s 2s 2p^2(2), 2p^4, 2s 2p^2 3d(3)$	7	−25.268	−25.337		
4	^1D	$2s^2 2p^2$	$1s 2s 2p^2, 2p^4, 2s 2p^2 3d(3)$	6	−25.122	−25.205		
4	^1S	$2s^2 2p^2$	$1s 2s 2p^2, 2p^4, 2s 2p^2 3d$	4	−24.998	−25.101		
4	$^3D^o$	$2s 2p^3$	$1s 2p^3, 2s^2 2p 3d$	3	−24.892	−25.966		
4	$^3P^o$	$2s 2p^3$	$1s 2s^2 2p, 1s 2p^3, 2s^2 2p 3d$	4	−24.743	−24.832		
5	$^4S^o$	$2s^2 2p^3$	$1s 2s 2p^3(2), 2s 2p^3 3d$	4	−28.791	−28.891		
5	^4P	$2s 2p^4$	$1s 2s^2 2p^2, 1s 2p^4, 2s^2 2p^2 3d, 2p^4 3d$	5	−28.362	−28.477		

[a] Number of different coupling schemes is given in parentheses.
[b] Moore (Ref. 30).
[c] Safranova and Kharitonova (Ref. 39), but corrected for relativistic effects.
[d] CI calculation by Holøien and Geltman (Ref. 40), but corrected for relativistic effects.
[e] CI calculation by Ahmed and Lipsky (Ref. 41), but corrected for relativistic effects.

$$E[\mathrm{O}(1s2s^1S)3s^2S]$$
$$= 3/4E(\mathrm{F}1s^22s3s^3S) + 1/4E(\mathrm{F}1s^22s3s^1S)$$
$$- E(\mathrm{F}1s^22s) + E(\mathrm{O}1s2s^1S)$$
$$+ (\langle 3s|1/r - J_{1s}|3s\rangle + 1/2K_{1s3s}) \quad (4b)$$

Estimated Auger transition energies associated with initial $1s2lnl'$ $(n=3,4)$ states in Li-like oxygen are presented in Table IV. The Δ_{SCF} corrections are of the order 0–2.5 eV for $n=3$ and decrease rapidly for larger Rydberg quantum numbers.

In Table IV we compare our results to those of Junker and Bardsley[42] and Holøien and Geltman.[40] The data of Holøien and Geltman were corrected for relativistic effects. We see that the predictions of Junker and Bardsley are up to 2 eV too high.

V. LINE IDENTIFICATION

A. Prompt spectra

1. 5-MeV spectra

A representative projectile Auger spectrum obtained for 5-MeV O^{2+} → C-foil collisions is shown in Fig. 8. The main peaks are numbered 1′ to 21′ in the order of increasing energy. Calibration of ionic rest frame energies was achieved by using the $(1s2s^2)^2S \rightarrow (1s^2\epsilon s)^2S$ transition energy.

Figures 9 and 10 are partial energy diagrams of Li-like and Be-like singly core-excited states. In Table V experimental peak energies are tabulated together with predicted transition energies between 424 and 535 eV.

It is evident from Fig. 8 that the prompt Auger spectrum is composed of two basic line structures around 430 and 490 eV. According to Figs. 9 and 10 and Table V the prominent lines in the first peak group may be identified as being due to singly core-excited Li-like and Be-like systems. Specifically, the lowest energy line at 412.6 eV is attributed to the initial $(1s2s^2)^2S$ state in Li-like oxygen. The high-energy tail of this line at about 416 eV originates from the decay of the metastable $(1s2s2p)^4P^0$ term.

Peak 1′ can be identified as the $\mathrm{OV}(1s^22p)^3P^0 \rightarrow (1s^22p\epsilon s)^3P^0$ and the $\mathrm{OVI}1s(2s2p^3P^0)^2P^0 \rightarrow (1s^2\epsilon p)^2P^0$ transitions. We further note that the structure near 428 eV *(peak 2′)* may be associated with the decay of the initial $(1s2s^22p)^1P^0$ and $(1s2s2p^2)^5P$ states in OV. The next higher lying spectral feature, namely, *peak 3′* is assigned to the $\mathrm{OVI}1s(2s2p^1P^0)^2P^0$ initial state. *Peak 4′* at about 435 eV is a blend of Auger lines arising from the initial $\mathrm{OVI}(1s2p^2)^2D$, $\mathrm{OIV}(1s2s^22p^2)^2S$, $\mathrm{OIV}(1s2s^22p^2)^4P$, $\mathrm{OV}(1s2s^22p)^3P^0$, $\mathrm{OV}(1s2s2p^2)^3_aP$ and $\mathrm{OV}(1s2s2p^2)^3D$ states. *Peak 5′* is mainly at-

TABLE IV. Energies of Auger electrons from $1s2lnl'$ $(n=3,4)$ states of O^{5+} according to the equivalent core model compared with other theoretical data (energies in eV).

State	ECM [a]	GBT [b] MC	JB [c]	HG [d] Corr.
$1s2s3s\,^4S$	497.8	498.0	500.2	498.0
$1s2s3s\,^2_aS$	500.5	500.9		
$1s2s3p\,^4P^o$	502.2		503.9	502.3
$1s2s3s\,^2_aP^o$	502.7			
$1s2s3d\,^4D$	504.7		505.8	
$1s2s3s\,^2_bS$	506.2	506.6		
$1s2s3d\,^2_aD$	506.1			
$1s2p3s\,^4P^o$	506.8		508.2	508.0
$1s2p3s\,^2_aP^o$	509.1			
$1s2p3p\,^4D$	509.5		510.0	
$1s2s3p\,^2_bP^o$	509.9			
$1s2p3p\,^2_aP$	510.1		510.2	
$1s2p3p\,^4S$	510.5		511.1	511.4
$1s2p3d\,^4F^o$	511.1		511.8	
$1s2p3p\,^4P$	511.3		511.5	511.2
$1s2p3p\,^2_aD$	512.4			
$1s2p3d\,^2_aD^o$	512.2		512.3	
$1s2s3d\,^2_bD$	512.7			
$1s2p3d\,^4D^o$	513.2		513.5	
$1s2p3p\,^2_aS$	513.5			
$1s2p3d\,^4P^o$	513.8		514.5	
$1s2p3d\,^2_aF^o$	514.1			
$1s2p3d\,^2_aP^o$	515.5			
$1s2p3p\,^2_bD$	515.8			
$1s2p3p\,^2_bP$	516.2		516.8	
$1s2p3p\,^2_bS$	516.8			
$1s2p3d\,^2_bF^o$	517.4			
$1s2p3s\,^2_bP^o$	518.2			
$1s2p3d\,^2_bD^o$	518.2		518.4	
$1s2p3d\,^2_bP^o$	519.7			
$1s2s4s\,^4S$	526.7		529.9	527.6
$1s2s4s\,^2_aS$	527.6			
$1s2s4p\,^4P^o$	528.7		530.8	
$1s2s4p\,^2_aP^o$	528.9			
$1s2s4d\,^4D$	529.7		531.8	
$1s2s4d\,^2_aD$	530.1			
$1s2s4s\,^2_bS$	534.5			
$1s2p4s\,^4P^o$	534.8		535.9	
$1s2p4s\,^2_aP^o$	535.4			
$1s2p4p\,^4D$	536.0		536.4	

TABLE IV. (*Continued*)

State	ECM[a]	GBT[b] MC	JB[c]	HG[d] Corr.
$1s2p4p\,^2_aP$	536.1		536.8	
$1s2s4p\,^2_bP^o$	536.3			
$1s2p4p\,^4S$	536.5		536.9	
$1s2p4p\,^4P$	536.6		537.1	539.5
$1s2p4d\,^4F^o$	536.7		537.3	
$1s2p4p\,^2_aD$	536.9			
$1s2p4d\,^2_aD^o$	537.2		537.4	
$1s2p4p\,^2_aS$	537.4			
$1s2s4d\,^2_bD$	537.4			
$1s2p4d\,^4D^o$	537.5		537.8	
$1s2p4d\,^4P^o$	537.8		538.1	
$1s2p4d\,^2_aF^o$	537.9			
$1s2p4d\,^2_aP^o$	538.3			
$1s2p4s\,^2_bP^o$	540.2			
$1s2p4p\,^2_bD$	541.6			
$1s2p4p\,^2_bP$	541.8		542.3	
$1s2p4p\,^2_bS$	542.1			
$1s2p4d\,^2_bF^o$	542.4			
$1s2p4d\,^2_bD^o$	542.8		543.0	
$1s2p4d\,^2_bP^o$	543.3			

[a] Equivalent core model (this work).
[b] Generalized Brillouin-theorem multiconfiguration method (this work).
[c] Estimates of Junker and Bardsley (Ref. 42).
[d] Values based on the calculations of Holøien and Geltman (Ref. 40), but corrected for relativistic effects.

tributed to the $(1s2s^22p)\,^1P^0 \rightarrow (1s^22s\epsilon p)\,^1P^0$ transition. A possible explanation for *peak 6'* may be Auger decays associated with the initial $(1s2s2p^2)\,^3S$, $(1s2p^2)\,^2S$, $(1s2s2p^2)\,^1D$, and

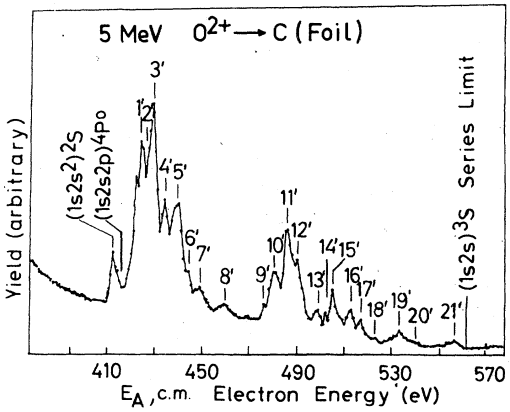

FIG. 8. High-energy portion of the 5-MeV $O^{2+} \rightarrow C$ (foil) electron energy spectrum (see Table V).

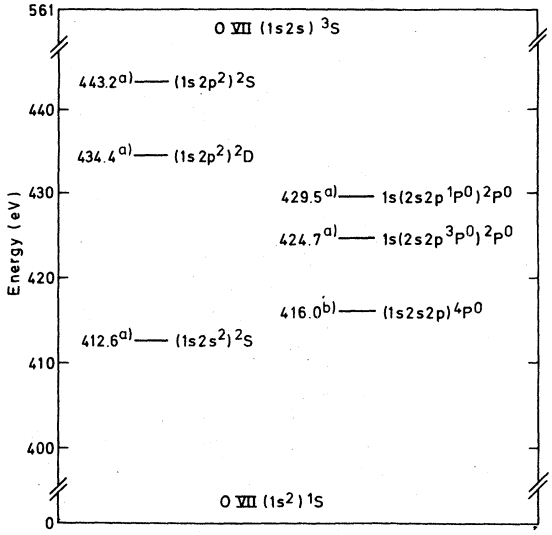

FIG. 9. Partial energy-level diagram of singly core-excited states in O VI. All energies are in eV. The zero of the energy scale is the energy of the O VII $(1s^2)\,^1S$ ground state. (a) Goldsmith; (b) experimental value (this work).

$(1s2s2p^2)\,^3_bP$ states (see Table V). *Peaks 7' and 8'* might be due to initial $(1s2s2p^2)\,^3D$ and $(1s2s2p^2)\,^1S$ states in Be-like oxygen, respectively.

According to Table V the dominant features (labeled 9'–13') in the second peak group (see Fig. 8) may be interpreted as contributions from doubly core-excited states in O VII, O VI, and O V. *Peak 11'* probably originates from initial $2s^22p$ and $2s^22p^2$ configurations. The creation of doubly core-excited states in the 5-MeV O^{2+}–C-foil excitation process is also confirmed by the predicted double

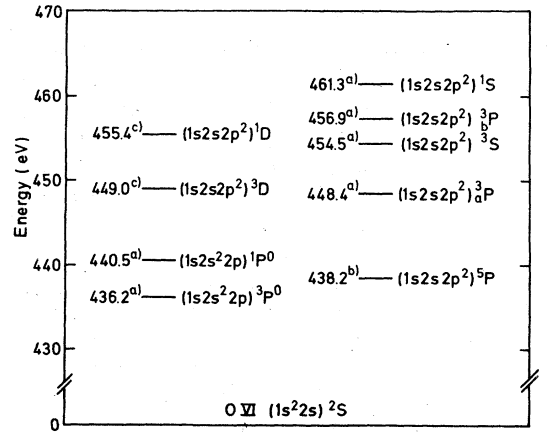

FIG. 10. Partial energy-level diagram of singly core-excited states in O V. All energies are in eV. The zero of the energy scale is the energy of the O VI $(1s^22s)^2S$ ground state. (a) = CI calculation (this work); (b) experimental value (this work); (c) estimated value (this work).

TABLE V. List of predicted Auger transition energies of numerous doubly core-excited and singly core-excited states. Comparison is made with experimental peak energies of the most prominent peaks in the 5- and 2-MeV projectile electron spectra.

	THEORY			EXPERIMENT			
				5-MeV spectra		2-MeV spectra	
Initial charge state	Initial state	Final state	Predicted transition energy	Peak number (Fig. 8)	Peak energy (eV)	Peak number (Fig. 8)	Peak energy (eV)
0^{4+}	$(1s2s^22p)^3P^0$	$(1s^22p\epsilon s)^3P^0$	424.2[a]			1	424 ± 1[a]
0^{5+}	$1s(2s2p^3P^0)^2P^0$	$(1s^2\epsilon p)^2P^0$	424.7[b]	1′	425 ± 1[a]		
0^{4+}	$(1s2s2p^2)^5P$	$(1s^22p\epsilon p)$	426.7[a]				
0^{4+}	$(1s2s^22p)^1P^0$	$(1s^22p\epsilon s)^1P^0$	428.5[a]	2′	428 ± 1[a]	2	428 ± 1[a]
0^{5+}	$1s(2s2p^1P^0)^2P^0$	$(1s^2\epsilon p)^2P^0$	429.5[c]	3′	430 ± 1[a]		
0^{5+}	$(1s2p^2)^2D$	$(1s^2\epsilon d)^2D$	434.4[b]				
0^{3+}	$(1s2s^22p^2)^2S$	$(1s^22p^2(^1S)\epsilon s)^2S$	434.8[a]	4′	435 ± 1[a]	3	435.5 ± 2[a]
0^{3+}	$(1s2s^22p^2)^4P$	$(1s^22p^2(^3P)\epsilon s)^4P$	435.7[a]				
0^{4+}	$(1s2s^22p)^3P^0$	$(1s^22s\epsilon p)^3P^0$	436.2[a]				
0^{4+}	$(1s2s2p^2)^3_aP$	$(1s^22p\epsilon p)^3P$	436.4[a]				
0^{4+}	$(1s2s2p^2)^3D$	$(1s^22p\epsilon p)^3D$	437.0[a]				
0^{4+}	$(1s2s2p^2)^5P$	$(1s^22s\epsilon s)$	438.7[a]				
0^{4+}	$(1s2s^22p)^1P^0$	$(1s^22s\epsilon p)^1P^0$	440.5[a]	5′	440 ± 2[a]		
0^{3+}	$(1s2s^22p^2)^2P$	$(1s^22p^2(^3P)\epsilon s)^2P$	441.5[a]				
0^{4+}	$(1s2s2p^2)^3S$	$(1s^22p\epsilon p)^3S$	442.5[a]				
0^{5+}	$(1s2p^2)^2S$	$(1s^2\epsilon s)^2S$	443.2[a]			4	443 ± 2[a]
0^{4+}	$(1s2s2p^2)^1D$	$(1s^22p\epsilon p)^1D$	443.4[a]	6′	444 ± 1[a]		
0^{4+}	$(1s2s2p^2)^3_bP$	$(1s^22p\epsilon p)^3P$	444.9[a]				

TABLE V. (*Continued*)

Initial charge state	THEORY Initial state	THEORY Final state	Predicted transition energy	EXPERIMENT 5-MeV spectra Peak number (Fig. 8)	5-MeV spectra Peak energy (eV)	2-MeV spectra Peak number (Fig. 8)	2-MeV spectra Peak energy (eV)
0^{3+}	$(1s2s^22p^2)^2D$	$(1s^22s2p(^1P^0)\epsilon p)^2D$	447.5[a]				
0^{3+}	$(1s2s^22p^2)^2P$	$(1s^22s2p(^1P^0)\epsilon p)^2P$	448.3[a]				
0^{4+}	$(1s2s2p^2)^3D$	$(1s^22s\epsilon d)^3D$	449.0[a]	7′	449 ± 1[a]	5	448.5 ± 1[a]
0^{4+}	$(1s2s2p^2)^1S$	$(1s^22p\epsilon p)^1S$	449.3[a]				
0^{3+}	$(1s2s2p^3)^2_aP^0$	$(1s^22p^2(^1S)\epsilon p)^2P^0$	449.7[a]				
0^{3+}	$(1s2s^22p^2)^2S$	$(1s^22s2p(^1P^0)\epsilon p)^2S$	450.8[a]				
0^{3+}	$(1s2s^22p^2)^4P$	$(1s^22s2p(^3P^0)\epsilon p)^4P$	452.0[a]				
0^{3+}	$(1s2s2p^3)^4P^0$	$(1s^22p^2(^3P^0)\epsilon p)^4P$	452.1[a]				
0^{3+}	$(1s2s2p^3)^2_aD^0$	$(1s^22p^2(^1D)\epsilon p)^2D^0$	453.1[a]				
0^{4+}	$(1s2s2p^2)^3S$	$(1s^22s\epsilon s)^3S$	454.5[a]			6	454 ± 1[a]
0^{3+}	$(1s2s2p^3)^2_bP^0$	$(1s^22p^2(^1S)\epsilon p)^2P^0$	455.0[a]				
0^{3+}	$(1s2s2p^3)^2_aD^0$	$(1s2p^2(^3P)\epsilon p)^2D^0$	455.3[a]				
0^{4+}	$(1s2s2p^2)^1D$	$(1s^22s\epsilon d)^1D$	455.4[a]			7	457 ± 2[a]
0^{4+}	$(1s2s2p^2)^1S$	$(1s^22s\epsilon s)^1S$	461.3[a]	8′	460 ± 2[a]		
0^{6+}	$(2s^2)^1S$	$(1s\epsilon s)^1S$	462.3[a]			8	463 ± 2[a]
0^{6+}	$(2s2p)^3P^0$	$(1s\epsilon p)^3P^0$	464.4[a]			9	466 ± 2[a]
0^{5+}	$(2s^22p)^2P^0$	$(1s2p(^1P^0)\epsilon s)^2P^0$	473.6[a]				
0^{6+}	$(2p^2)^1D$	$(1s\epsilon d)^1D$	474.8[a]			10	~471[a]
0^{6+}	$(2s2p)^1P^0$	$(1s\epsilon p)^1P^0$	476.0[d]	9′	477 ± 2[a]		
0^{5+}	$(2s^22p)^2P^0$	$(1s2p(^3P^0)\epsilon s)^2P^0$	478.9[d]				
0^{5+}	$(2s^22p)^2P^0$	$(1s2s(^1S)\epsilon p)^2P^0$	478.9[d]	10′	481 ± 2[a]	11	~481[a]
0^{4+}	$(2s^22p^2)^1S$	$(1s2p^2(^2S)\epsilon s)^1S$	483.6[a]			12	~484[a]
0^{4+}	$(2s^22p^2)^3P$	$(1s2p^2(^2P)\epsilon s)^3P$	485.3[a]				
0^{5+}	$(2s^22p)^2P^0$	$(1s2s(^3S)\epsilon p)^2P^0$	486.5[d]	11′	486 ± 2[a]		
0^{5+}	$(2s2p^2)^2S$	$(1s2p(^1P^0)\epsilon p)^2S$	490.2[d]	12′	490 ± 2[a]		
0^{4+}	$(2s^22p^2)^1D$	$(1s2p^2(^2D)\epsilon s)^1D$	490.5[a]				
0^{4+}	$(2s^22p^2)^3P$	$(1s2p^2(^4P)\epsilon s)^3P$	492.0[a]				
0^{5+}	$(2s2p^2)^2S$	$(1s2p(^3P^0)\epsilon p)^2S$	495.5[a]				

TABLE V. (*Continued*)

Initial charge state	THEORY Initial state	THEORY Final state	Predicted transition energy	EXPERIMENT 5-MeV spectra Peak number (Fig. 8)	EXPERIMENT 5-MeV spectra Peak energy (eV)	EXPERIMENT 2-MeV spectra Peak number (Fig. 8)	EXPERIMENT 2-MeV spectra Peak energy (eV)
O^{5+}	$(2s2p^2)^2S$	$(1s2s(^1S)\epsilon s)^2S$	495.5[a]				
O^{4+}	$(2s^22p^2)^1S$	$(1s2s2p(^2_bP^0)\epsilon p)^1S$	498.2[a]	13′	498 ± 2[a]	13	~497[a]
O^{5+}	$(1s2s3s)^2_aS$	$(1s^2\epsilon s)^2S$	500.5[a]				
O^{5+}	$(1s2s3p)^2_aP^0$	$(1s^2\epsilon p)^2P^0$	502.7[a]	14′	502.5 ± 2[a]	14	~502[a]
O^{4+}	$(2s^22p^2)^1S$	$(1s2s2p(^2_aP^0)\epsilon p)^1S$	502.9[a]				
O^{5+}	$(2s2p^2)^2S$	$(1s2s(^3S)\epsilon s)^2S$	503.1[a]				
O^{4+}	$(2s^22p)^3P$	$(1s2s2p(^4P^0)\epsilon p)^3P$	505.0[a]	15′	505 ± 2[a]		
O^{5+}	$(1s2s3d)^2_aD$	$(1s^2\epsilon d)^2D$	506.1[a]				
O^{5+}	$(1s2s3s)^2_bS$	$(1s^2\epsilon s)^2S$	506.2[a]				
O^{5+}	$(1s2p3s)^2_aP^0$	$(1s^2\epsilon p)^2P^0$	509.1[a]				
O^{5+}	$(1s2s3p)^2_bP^0$	$(1s^2\epsilon p)^2P^0$	509.9[a]				
O^{4+}	$(2s^22p^2)^1D$	$(1s2s^2(^2S)\epsilon d)^1D$	512.1[a]			15	~512[a]
O^{5+}	$(1s2p3p)^2_aD$	$(1s^2\epsilon d)^2D$	512.4[a]				
O^{5+}	$(1s2s3d)^2_bD$	$(1s^2\epsilon d)^2D$	512.7[a]	16′	512.5 ± 2[a]		
O^{5+}	$(1s2p3p)^2_aS$	$(1s^2\epsilon s)^2S$	513.5[a]				
O^{5+}	$(1s2p3p)^2_aF^0$	$(1s^2\epsilon f)^2F^0$	514.1[a]				
O^{4+}	$(2s^22p^2)^1S$	$(1s2s^2(^2S)\epsilon s)^1S$	515.0[a]				
O^{4+}	$(2s2p^3)^3D^0$	$(1s2s2p(^4P^0)\epsilon d)^3D^0$	515.1[a]				
O^{5+}	$(1s2p3d)^2_aP^0$	$(1s^2\epsilon p)^2P^0$	515.5[a]				
O^{5+}	$(1s2p3p)^2_bD$	$(1s^2\epsilon d)^2D$	515.8[a]				
O^{5+}	$(1s2p3p)^2_bS$	$(1s^2\epsilon s)^2S$	516.8[a]	17′	517 ± 2[a]		
O^{5+}	$(1s2p3d)^2_bF^0$	$(1s^2\epsilon f)^2F^0$	517.2[a]				
O^{5+}	$(1s2p3s)^2P^0$	$(1s^2\epsilon p)^2P^0$	518.2[a]				
O^{4+}	$(2s2p^3)^3P^0$	$(1s2s2p(^4P^0)\epsilon d)^3P^0$	518.8[a]			16	~519[a]
O^{4+}	$(2s2p^3)^3P^0$	$(1s2s2p(^4P^0)\epsilon s)^3P^0$	518.8[a]				
O^{5+}	$(1s2p3d)^2_bP^0$	$(1s^2\epsilon p)^2P^0$	519.7[a]				
O^{3+}	$(2s^22p^3)^4S^0$	$(1s2s2p^2(^5P)\epsilon p)^4S^0$	524.0[a]	18′	~523[a]		

TABLE V. (*Continued*)

Initial charge state	THEORY Initial state	Final state	Predicted transition energy	EXPERIMENT 5-MeV spectra Peak number (Fig. 8)	5-MeV spectra Peak energy (eV)	2-MeV spectra Peak number (Fig. 8)	2-MeV spectra Peak energy (eV)
O^{5+}	$(1s2s4s)^2_aS$	$(1s^2\epsilon s)^2S$	527.6[a]	17	~528[a]		
O^{5+}	$(1s2s4p)^2_aP^0$	$(1s\epsilon p)^2P^0$	528.9[a]				
O^{5+}	$(1s2s4d)^2_aD$	$(1s^2\epsilon d)^2D$	530.1[a]				
O^{5+}	$(1s2s4s)^2_bS$	$(1s^2\epsilon s)^2S$	534.5[a]	19′	~533[a]		
O^{3+}	$(2s^22p^3)^4P$	$(1s2s2p^2(^5P)\epsilon p)^4P$	535.2[a]				

[a] This work.
[b] Goldsmith (Ref. 37).
[c] Safronova and Kharitonova (Ref. 39).
[d] Ahmed and Lipsky (Ref. 41).

to single oxygen K-vacancy production ratio (see Sec. VI).

Above 500.5 eV corresponding to the $OVI(1s2s3s)^2_aS \rightarrow (1s^2\epsilon s)^2S$ Auger transition (see Table V), decays from single core-excited $1s2lnl$ $(n \geq 3)$ states in OVI may overlap with transitions from doubly core-excited states. For example *peak 16′* centered at 512.5 eV might be a blend of lines arising from initial $1s2l3l'$ states in OVI and the $OV(2s^22p^2)^1D \rightarrow [1s2s^2(^2S)\epsilon d]^1D$ transition. Finally, we note that above the $(1s2s)^3S \infty l \rightarrow 1s^2\epsilon s$ series limit at 561.0 eV, no pronounced structure occurs.

2. 2-MeV spectra

Figure 6 shows typical ejected electron spectra observed for (i) 2-MeV $O^+ \rightarrow$ Ne and (ii) 2-MeV $O^+ \rightarrow$ C-foil excitation. The energy scale was normalized to the $OVI(1s2s^2)^2S \rightarrow (1s^2\epsilon s)^2S$ transition. The main peaks in the spectra shown in Fig. 6 have been given numbers to facilitate reference to Table V.

At 2-MeV beam energy the projectile Auger spectra are expected to be dominated by four-, five-, and six-electron oxygen ions. The analysis of the 2-MeV oxygen spectra are complicated by the possibility of highly excited B-like and C-like levels decaying to more than one final ion state. A typical energy level diagram illustrating the Auger decay channels of the $(1s2s^22p^2)\ ^4P$, ^2D, ^2P, and ^2S terms in OVI is indicated in Fig. 11. For example the B-like $(1s2s^22p^2)^4P$ term decays to the $(1s2p^2)^3P$ and the $(1s^22s2p)^3P^0$ final ionic states resulting in ejected electrons of 435.7 and 452.0 eV, respectively.

The lowest-energy line in each of the 2-MeV spectra is identified as corresponding to Auger electron transitions from the $(1s2s^2)^2S$ and the $(1s2s2p)^4P^0$ states in Li-like oxygen. The next-higher-lying Auger feature labeled 1 is mainly associated with the $(1s2s^22p)^3P^0 \rightarrow (1s^2p\epsilon s)^3P^0$ transition in Be-like oxygen. *Peak 2* is attributed predominantly to the $OV(1s2s^22p)^1P^0 \rightarrow (1s^22p\epsilon s)^1P^0$ decay, consistent with a predicted energy of 428.5 eV. *Line 3* is relatively intense and may be attributed to excitation of $(1s2s^22p)^2S$ and ^4P in B-like OIV and of $(1s2s^22p)^3P^0$ and $(1s2s^22p^2)^3_aP$ in B-like OV. The estimated position of *line 4* is 443.0 eV. In this region there may be several transitions originating from Li-, Be-, and B-like states. *Line 5* is ascribed to singly core-excited states in OIV and OV. *Peak 6* is attributed to blends of transitions from several states of four- and five-electron oxygen ions. For the remaining lines no detailed discussion can be given. It is likely that *line 7* results from single K-vacancy states in Be-, and B-like oxygen. Peaks 8–13 may be associated

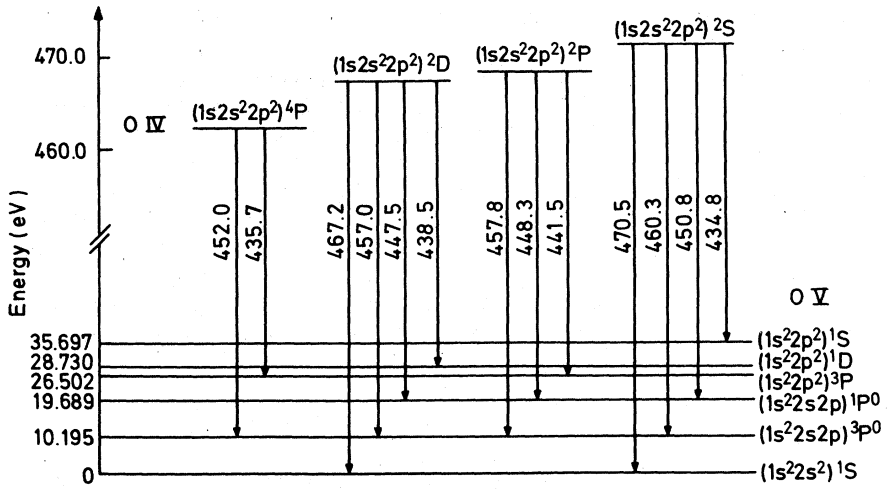

FIG. 11. Partial energy-level diagram showing Auger decays originating from initial singly core-excited states in O IV. All energies are in eV. The zero of the energy scale is the energy of the O V $(1s^2 2s^2)^1S$ ground state.

with double K-vacancy states. The spectral region above 500.5 eV *(lines 14–18)* is due to double K-vacancy states in OV, OIV, and OIII and due to lines originating from OVI$(1s2lnl')$ $(n \geq 3)$ excitation processes. This is supported by a predicted double to single oxygen K-vacancy-production ratio of about 6% and 1.5% for 2-MeV oxygen on neon and solid carbon, respectively (see Sec. VI).

Examination of Fig. 6 also reveals that the main spectral features observed for (i) 2-MeV O^+–Ne and (ii) 2-MeV O^+–C-foil impact, show little variation in relative line intensities, i.e., nearly the same initial states are created in both collision systems.

B. Delayed spectra

Figure 7 is a plot of prompt and delayed projectile Auger spectra observed for 5-MeV O^{2+}–C-foil excitation. The delayed spectral features can be assigned primarily to initial singly core-excited states in Li-like and Be-like oxygen. Thus, the lowest energy peak (labeled 1) is attributed to the Auger decay of the metastable $(1s2s2p)^4P^0$ term in OVI. From the present work we deduce a transition energy of 416.0 ± 1 eV for the OVI$(1s2s2p)^4P^0$ level. *Peak 2* is unresolved due to the close proximity of transitions arising from the OVI$(1s2p^2)^4P$ and the OV$(1s2s2p^2)^5P$ initial states. Due to the competing optical decay channel [i.e., $(1s2s2p)^4P^0 - (1s2p^2)^4P$] the $(1s2p^2)^4P$ terms should be dominantly deexcited via $E1$ transitions.[43] It is therefore assumed that the $(1s2p^2)^4P$ levels are almost entirely depleted after a time of flight of a few nanoseconds.

The third strong line (labeled *3*) at about 438.5 eV is identified as the $(1s2s2p^2)^5P$ state decaying to the $(1s^2 2s)^2S$ final ionic state. We further note that the weaker feature *(peak 4)* at about 445 eV may originate from the $(1s2p^3)^5S^0$ state in OV. This state should be depleted preferentially via electric dipole transition [i.e., $-(1s2s2p^2)^5P$ $(1s2p^3)^5S^0$. It is expected that peaks (labeled *5–9*) are due to initial OVI$(1s2lnl')$ states with the nl' electron being excited into the $n=3$ shell or higher (see Table IV). Above the three electron $(1s2s)^3$ series limit (label 10) at 561.0 eV no additional autoionization lines were observed.

In Table VI we present a comparison of our data with those of Pegg *et al.*,[16] Forester *et al.*,[44] Goldsmith,[37] Safronova and Kharitonova,[39] and Junker and Bardsley.[42] We find reasonable agreement between our calculations and the experimental energies obtained in this work. When comparing our calculations with those of Junker and Bardsley deviations larger than 1 eV occur. Finally, we find good agreement between our experimental results and the work of Forester *et al.*[44]

VI. EXCITATION AND DEEXCITATION MECHANISM

A calculation of the production cross sections for the multiply ionized excited states which have been resolved in this work lies outside the capability of available theoretical approaches. A recent approach due to Bottcher[45] does not apply in the present situation since it requires collision velocities well above electron orbital velocities. In violent collisions as those considered here, so many excitation, ionization, and charge-exchange channels are accessible, in particular for outer shell electrons, that it is unfeasible to account theoretically for the relative populations of the various excited configurations and the corresponding LS components. It is relatively easier to calculate the basic cross section for vacancy production in the relevant projectile or target-atom inner shells. In

TABLE VI. Ejected-electron energies corresponding to Auger transitions from Li-like $(1s2s2p)^4P^o$ and $(1s2s2p^2)^5P$ states. Comparison is made with earlier experimental and theoretical results.

Peak number	Initial state	Final ionic state	Transition Energy (eV) experiment	theory
1	$(1s2s2p)^4P^o$	$(1s^2)^1S$	417[a]	417.3[b]
			416.2 ± 0.5[c]	417.0[d]
			416.0 ± 1[e]	416.9[f]
				416.2[g]
2	$(1s2s2p^2)^5P$	$(1s^22p)^2P^o$	425, 427[a]	428.3[b]
			426.4 ± 0.5[c]	427.6[f]
			426.2 ± 1[e]	426.7[e]
	$(1s2p^2)^4P$	$(1s^2)^1S$	429[a]	429.5[b]
			429.4 ± 0.5[c]	429.3[g]
			429.1 ± 1[e]	
3	$(1s2s2p^2)^5P$	$(1s^22s)^2S$	440[a]	440.3[b]
			438.7 ± 0.5[c]	439.6[f]
			438.2 ± 1[e]	438.7[e]

[a] Pegg *et al.* (Ref. 16).
[b] Junker and Bardsley (Ref. 42).
[c] Forester *et al.* (Ref. 44).
[d] Holøien and Geltman (Ref. 40).
[e] This work.
[f] Safronova and Kharitonova (Ref. 39).
[g] Goldsmith (Ref. 37).

the present study, a theoretical estimate of the ratio of the cross sections for single and double K-vacancy production is important for the line identification, especially in the spectral region with strong overlap of lines resulting from the decay of single and double K-vacancy configurations (see Sec. V).

A quasimolecular description[46] is appropriate for these collision systems in order to account for the strong interaction of either nucleus with the electrons cloud of the other partner. This approach is particularly suited in slow collisions where electron orbitals may relax almost adiabatically in response to the variation of the combined field during the encounter. Then only a few channels may be needed in the calculation. A simple description of K-shell excitation processes in terms of the $1s\sigma$, $2p\sigma$, and $2p\pi$ molecular orbitals (MO) (see Fig. 12) has proven its validity in a variety of examples of nearly symmetric collisions systems.[47] The basic process in this model is the $2p\sigma$-$2p\pi$ rotational coupling. Considering that the $2p\pi$ orbital is not fully occupied at small separations of the nuclei, this coupling may result in the production of one or two $2p\sigma$ vacancies. Subsequently, the radial coupling between the $1s\sigma$ and $2p\sigma$ MO may distribute these vacancies over the two K shells of the collision partners. Universal expressions and scaling rules for these processes are available.[48,49]

In the present experiments of 2- and 5-MeV oxygen impact on neon and carbon the collision velocity is not much smaller than the relevant electron orbital velocities. Since this is usually considered to be a requirement for the applicability of a few state MO description, it may be questioned whether such a simple treatment is valid. It is, on the other hand, the only available model which cannot be ruled out beforehand. First, we consider the O +Ne case.

Since the $2p$ subshell of the Ne target atom is fully occupied, initially there is no vacancy available in the $2p\pi_x$ orbital. (Referring to a frame with

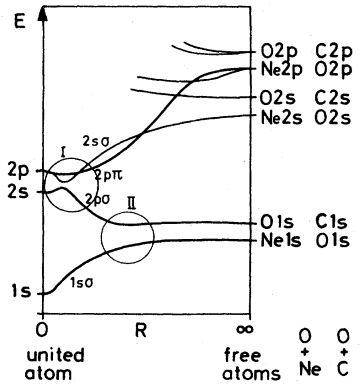

FIG. 12. Schematic diagram of the orbital energies in the O+Ne and O+C systems. Bold lines indicate those orbitals which are most significant for k-vacancy production. Region I; dominant $2p\pi$-$2p\sigma$ rotational coupling, and weak $2s\sigma$-$2p\sigma$ radial coupling. Region II: $2p\sigma$-$1s\sigma$ radial Demkov coupling.

x axis in the collision plane and perpendicular to the internuclear axis, only the $2p\pi_x$ component may couple to the $2p\sigma$ MO). However, $2p\pi_x$ vacancies may be generated dynamically at intermediate separations by coupling to higher vacant MO's or to the continuum. Assuming that the probability for this process is t, per $2p\pi_x$ electron, the probabilities p_I and p_{II} that the $2p\pi_x$ orbital at small separations carries one and two vacancies, respectively, are given by

$$p_I = 2t(1-t), \quad p_{II} = t^2 . \tag{5}$$

Now let us define the cross sections

$$\sigma_I^{\rm rot} = 2\pi \int P(b)\, b\, db, \quad \sigma_{II}^{\rm rot} = 2\pi \int [P(b)]^2 b\, db \tag{6}$$

in terms of the impact-parameter-dependent probability $P(b)$ for a $2p\pi$-$2p\sigma$ transition per $2p\pi_x$ vacancy. The single and double $2p\sigma$ vacancy-production cross sections σ_I and σ_{II} may then be expressed as

$$\begin{aligned} \sigma_I &= p_I \sigma_I^{\rm rot} + 2p_{II}(\sigma_I^{\rm rot} - \sigma_{II}^{\rm rot}), \\ \sigma_{II} &= p_{II} \sigma_{II}^{\rm rot} . \end{aligned} \tag{7}$$

Inserting the expressions of Eq. (5) we obtain the following result for the single- to double-K-vacancy production ratio

$$\sigma_I/\sigma_{II} = (2/t)(\sigma_I^{\rm rot}/\sigma_{II}^{\rm rot}) - 2 . \tag{8}$$

The theoretical cross-section ratio on the right-hand side may be obtained from the tables of Taulbjerg *et al.*[48] For the parameter t we may employ semiempirical values determined by Bøving.[50] His results can be expressed in the parametrized form (using atomic units)

$$t^{-1} = 1 + e^{\alpha/v}, \tag{9}$$

where $\alpha = 1.55$ for the O+Ne system.

Ignoring the radial coupling between the $1s\sigma$ and $2p\sigma$ MO, Eq. (8) may be used to estimate the oxygen single- to double-K-vacancy production ratio in O+Ne collisions. However, in O+C collisions the $1s\sigma$-$2p\sigma$ interaction is as important as the $2p\pi$-$2p\sigma$ coupling since the oxygen K shell for this system is correlated with the $1s\sigma$ MO (see Fig. 12). Assuming that the probability of transferring a $2p\sigma$ vacancy into the $1s\sigma$ MO can be approximated by a constant w over the impact-parameter range that is relevant for the preceding $2p\pi$-$2p\sigma$ coupling, the cross sections σ_S and σ_D for single- and double-vacancy production in the $1s\sigma$ orbital (oxygen K shell) can be expressed as

$$\sigma_S = \sigma_I w + 2\sigma_{II} w(1-w), \quad \sigma_D = \sigma_{II} w^2 , \tag{10}$$

where σ_I and σ_{II} are given by Eqs. (6) and (7). But Eq. (5) does not apply in this situation. For 2- and 5-MeV oxygen projectiles in a solid, it is likely that the valence shell is stripped almost immediately upon penetration. Since the $2p$ orbital is correlated with the oxygen $2p$ subshell (see Fig. 12) we may then assume that

$$p_I = 0, \quad p_{II} = 1 . \tag{11}$$

Then we obtain

$$(\sigma_S/\sigma_D) = (2/w)(\sigma_I^{\rm rot}/\sigma_{II}^{\rm rot}) - 2 . \tag{12}$$

The vacancy-transfer probability w may be obtained from Meyerhof's expression,[49] i.e., from Eq. (9) with $w = t$ and $\alpha = \pi(\sqrt{2U_H} - \sqrt{2U_L})$, where U_H and U_L are the K-shell binding energies in atomic units of the higher- and lower-Z collision partner, respectively.

To summarize, we find that one may expect a double-to-single oxygen K-vacancy-production ratio of 6% and 1.5% for 2-MeV oxygen on neon and solid carbon, respectively. In case of 5-MeV oxygen impact the corresponding expectations are 7% and 3%, respectively. These estimates should now be compared with our experimental results as presented in Secs. III and V. According to Sec. V Auger electrons from doubly core-excited states can appear in the spectral region above 462 eV (see Table V) whereas singly core-excited states of the type $1s2ln'l'$ ($n \geq 3$) can occur above 498 eV (see Table IV). The measured ratio between the yield above 460 eV and the total yield of Auger electrons is about 10% in the neon gas case; i.e., the magnitude of the calculated cross-section ratio agrees within a factor of 2 with the experimental value. This supports the interpretation of Sec. V that doubly core-excited states contribute significantly to the high-energy Auger structure.

In case of oxygen excitation by carbon foils the predicted cross-section ratio is much smaller than the ratio between the experimental yield in the two spectral structures. One may think of several explanations of this. First, it is possible that some of the approximations employed in the above estimates become invalid. For example, it may be incorrect to use the same w to describe single as well as double-K-vacancy sharing. Second, multiple collision effects may play a significant role in the generation of doubly core-excited projectile states in a foil.[3,5,51,52] Third, the experimental data do not exclude that singly core-excited states may dominate the spectral structure above 498 eV at the expense of doubly core-excited states.

Finally we note that cascading processes[52] may introduce difficulties in the study of K-shell excitation mechanisms. For instance the O V$(2s^22p^2)^1D$ state can decay to the single core-excited O VI$(1s2s^2)^2S$ state which in turn populates the O VII$(1s^2)^1S$ ground state giving two ejected-electron

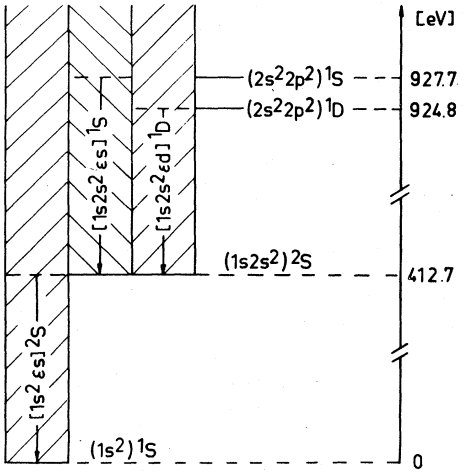

FIG. 13. Cascade feeding of the Li-like $(1s2s^2)^2S$ state in O VI via Auger decays originating from initially Be-like double-hole states in O V.

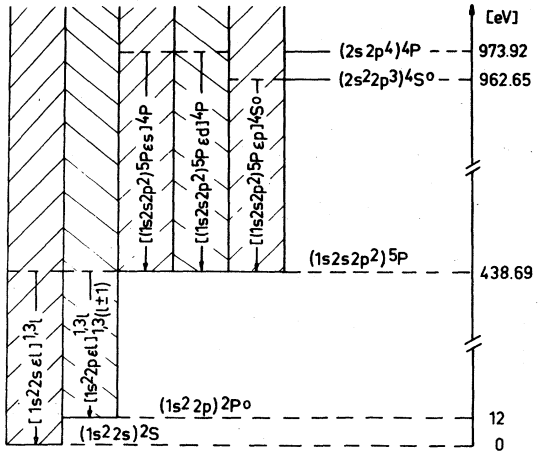

FIG. 15. Cascade feeding of the Be-like $(1s2s2p^2)^5P$ state in O V via Auger decays from initially B-like double-hole states in O IV.

energies of about 512.1 and 412.7 eV. This cascade process is illustrated in Fig. 13. Another typical cascade-feeding mechanism is depicted in Fig. 14. As can be seen the O V $(2s^22p^2)^3P$, $(2s2p^3)^3D$, and $(2s2p^3)^3P$ initial states decay to the metastable autoionizing Li-like $(1s2s2p)^4P^o$ term. Figure 15 shows Auger processes where the Be-like $(1s2s2p^2)^5P$ state is produced following the deexcitation of B-like double-K-vacancy states. From these examples it is clear that the Auger cascade mechanism may influence the production cross sections of singly core-excited states.

VII. SUMMARY AND CONCLUSION

Initial high-resolution measurements of Auger-electron emission spectra for oxygen-ion beams excited by single-collision gas- and multiple-collision foil excitation have been discussed and compared to theoretical calculations. Auger-electron spectra recorded at zero distance downstream from the collision region are dominated by prompt transitions, but the decay of metastable states is also observed due to the finite acceptance length of the spectrometer. For comparison with the beam-gas spectra, beam-foil Auger electron spectra were recorded as a function of distance downstream from a carbon exciter foil.

Increased multiple ionization and enhanced line broadening is found for heavier exciter gases and higher incident beam energies, but little incident-ion charge state dependence is detected. When spectra for 2-MeV oxygen beams are recorded with the analyzer directly viewing the collision region (i.e., at zero distance downstream), enhanced line broadening due to multiple collisions [$O^+ \rightarrow$ C-foil spectrum] is observed to be negligible compared to the broadening present for single ion-atom collisions ($O^+ \rightarrow$ Ne spectrum). This observation certainly deserves further investigation.

To study cross-section ratios of individual Auger lines the instrumental conditions must be improved. This can be realized by decreasing the range of θ_L due to finite acceptance angles of the electron spectrometer and selecting observation angles θ_L close to 0° or 180° with respect to the beam direction. In this manner a large number of hitherto unresolved Auger structures might be resolved. However, overlapping of Auger lines resulting from initial singly and doubly core-excited states may preclude unambiguous identification of specific lines on the basis of energy calculations alone. In order to facilitate the line interpretation

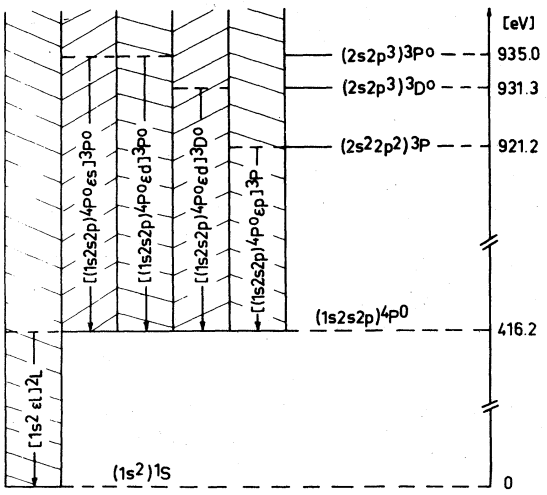

FIG. 14. Cascade feeding of the Li-like $(1s2s2p)^4P^0$ state in O VI via Auger decays from initially Be-like double-hole states in O V.

there is a need apparent for detailed Auger transition probability calculations of Li-, Be-, and C-like states.

ACKNOWLEDGMENTS

The authors wish to thank Professor C. F. Moore from the University of Texas at Austin for supporting the various experiments discussed in this contribution. Two of us (W.H.E.S. and M.M.) are grateful to Professor S. D. Peyerimhoff for the hospitality, to the Bonn University Computer Center for computing time, and to the Deutsche Forschungsgemeinschaft for financial support. Finally the authors are indebted to Professor W. Mehlhorn for helpful comments.

---

*Present address: Theoretical Chemistry, University, POB 210209, D-5900 Siegen 21, West Germany.

[1]D. L. Matthews, B. M. Johnson, J. J. Mackey, and C. F. Moore, Phys. Rev. Lett. 31, 1331 (1973).

[2]M. E. Rudd and J. H. Macek, *Case Studies in Atomic Physics 3*, edited by M. R. C. McDowell and E. W. McDaniel (North-Holland, Amsterdam, 1973), p. 47.

[3]H. G. Berry, Phys. Scr. 12, 5 (1975).

[4]N. Stolterfoht, Proceedings of the Fourth Conference on the Application of Small Accelerators, Denton, 1976, Publ. No. 76 CH 117-9 NTS, and references therein (unpublished).

[5]H. G. Berry, Rep. Prog. Phys. 40, 155 (1977).

[6]D. Schneider, R. Bruch, W. H. E. Schwarz, T. C. Chang, and C. F. Moore, Phys. Rev. A 15, 926 (1977).

[7]M. Rødbro, R. Bruch, and P. Bisgaard, J. Phys. B 10, L275 (1977).

[8]N. Stolterfoht, D. Schneider, R. Mann, and F. Folkmann, J. Phys. B 10, L281 (1977).

[9]R. Bruch, M. Rødbro, P. Bisgaard, and P. Dahl, Phys. Rev. Lett. 39, 801 (1977).

[10]D. Schneider, C. F. Moore, and B. M. Johnson, J. Phys. B 9, L153 (1976).

[11]D. L. Matthews, R. J. Fortner, D. Schneider, and C. F. Moore, Phys. Rev. A 14, 1561 (1976).

[12]P. Ziem, R. Bruch, and N. Stolterfoht, J. Phys. B 8, L480 (1975).

[13]N. Stolterfoht, Proceedings of the International Conference on Inner Shell Ionization Phenomena, Freiburg, 1976, edited by W. Mehlhorn and R. Brenn (unpublished), pp. 42–56.

[14]D. Schneider, K. Roberts, W. Hodge, and C. F. Moore, Phys. Rev. Lett. 17, 1065 (1976).

[15]N. Stolterfoht, D. Schneider, D. Burch, and J. S. Risley, Phys. Rev. Lett. 33, 59 (1974).

[16]D. J. Pegg, I. A. Sellin, R. Peterson, J. R. Mowat, W. W. Smith, M. D. Brown, and J. R. MacDonald, Phys. Rev. A 8, 1350 (1973).

[17]I. A. Sellin, Nucl. Instrum. Methods 110, 477 (1973).

[18]D. Schneider, W. Hodge, B. M. Johnson, L. E. Smith, and C. F. Moore, Phys. Lett. 54, 174 (1975).

[19]B. Rosner and D. Gur, Phys. Rev. A 15, 70 (1977).

[20]B. Rosner and W. Brandt, Phys. Lett. A 61, 97 (1977).

[21]N. Stolterfoht, D. Schneider, D. Burch, A. Aagaard, E. Bøving, and B. Fastrup, Phys. Rev. A 12, 1313 (1975).

[22]P. Dahl, M. Rødbro, B. Fastrup, and M. E. Rudd, J. Phys. B 9, 1567 (1976).

[23]B. M. Johnson, Ph.D. thesis (University of Texas at Austin, 1975) (unpublished).

[24]D. L. Matthews, B. M. Johnson, J. J. Mackey, L. E. Smith, W. Hodge, and C. F. Moore, Phys. Rev. A 10, 1177 (1974).

[25]M. O. Krause, T. A. Carlson, and W. E. Moddeman, J. Phys. (Paris) Colloq. C 4, 139 (1971).

[26]C. Froese-Fischer, Comput. Phys. Commun. 1, 151 (1969).

[27]D. L. Matthews, B. M. Johnson, and C. F. Moore, At. Data Nucl. Data Tables 15, 41 (1975).

[28]W. H. E. Schwarz, Proceedings of the International Conference on the Physics of X-ray Spectra, Gaithersburg, 1976, p. 49 (unpublished).

[29]K. Radler, B. Sonntag, T. C. Chang, and W. H. E. Schwarz, Chem. Phys. 13, 363 (1976).

[30]C. E. Moore, *Atomic Energy Levels*, NSRDS-NBS No. 35 (U. S. GPO, Washington, D. C., 1971).

[31]S. Bashkin and J. O. Stoner, *Atomic Energy Levels and Grotrian Diagrams* (North-Hollamd, Amsterdam, 1975).

[32]W. H. E. Schwarz and T. C. Chang, Int. J. Quantum Chem. S 10, 91 (1976).

[33]T. C. Chang and W. H. E. Schwarz, Theor. Chim. Acta 44, 45 (1977).

[34]F. B. van Diujenveldt, *Gaussian Basis Sets for the Atoms H-He for Use in Molecular Calculations* (IBM, San José, 1971).

[35]I. Öksüz and O. Sinanoğlu, Phys. Rev. 181, 42, 54 (1969).

[36]H. T. Doyle, Adv. At. Mol. Phys. 5, 337 (1969).

[37]S. Goldsmith, J. Phys. B 7, 2315 (1974).

[38]S. Fraga, J. Karwowski, and K. M. S. Saxena, *Handbook of Atomic Data* (Elsvier, Amsterdam, 1976).

[39]U. I. Safranova and V. N. Kharitonova, Opt. Spectrosc. 27, 300 (1969).

[40]E. Holøien and S. Geltman, Phys. Rev. 153, 81 (1967).

[41]M. Ahmed and L. Lipsky, Phys. Rev. A 12, 1176 (1975).

[42]B. R. Junker and J. N. Bardsley, Phys. Rev. A 8, 1345 (1973).

[43]K. X. To, E. J. Knystautas, R. Drounin, and H. G. Berry, *Beam-Foil Spectroscopy*, edited by I. A. Sellin and D. Pegg (Plenum, New York, 1976), p. 385–391.

[44]J. P. Forester, R. S. Peterson, P. M. Griffin, P. J. Pegg, H. H. Haselton, K. H.Liao, I. A. Sellin, J. R. Mowat, and R. S. Thoe, *Beam-Foil Spectroscopy*, edited by I. A. Sellin and D. J. Pegg (Plenum, New York, 1976), p. 451–459.

[45]C. Bottcher, J. Phys. B 10, L445 (1977).

[46]J. S. Briggs, Rep. Prog. Phys. 39, 217 (1976).

[47]W. E. Meyerhof and K. Taulbjerg, Ann. Rev. Nucl. Sci. 27, 279 (1977).

[48]K. Taulbjerg, J. S. Briggs, and J. Vaaben, J. Phys. B 9, 1351 (1976).

[49]W. E. Meyerhof, Phys. Rev. Lett. 31, 1341 (1973).

[50]E. G. Bøving, Ph.D. thesis (University of Aarhus,

1977 (unpublished).
[51]R. Bruch, G. Paul, and J. Andrä, Phys. Rev. A 12, 1808 (1975).
[52]R. Bruch, Thesis (University of Berlin, 1976) (unpublished).